Chinese Chemical Letters 32 (2021) 2038–2042

Contents lists available at ScienceDirect

Chinese Chemical Letters

journal homepage: www.elsevier.com/locate/cclet

Communication

In situ construction of oxygen-vacancy-rich $Bi^0@Bi_2WO_{6-x}$ microspheres with enhanced visible light photocatalytic for NO removal

Xiaoqian Xie[a], Qadeer-Ul Hassan[a], Huan Lu[b,*], Fei Rao[a], Jianzhi Gao[a,*], Gangqiang Zhu[a,*]

[a] *School of Physics and Information Technology, Shaanxi Normal University, Xi'an 710062, China*
[b] *School of Geography and Tourism, Shaanxi Normal University, Xi'an 710062, China*

ARTICLE INFO

Article history:
Received 8 July 2020
Received in revised form 3 September 2020
Accepted 3 October 2020
Available online 6 October 2020

Keywords:
Bi_2WO_6 microspheres
Oxygen vacancies
Bi metal
Photocatalytic reaction
In situ FTIR

ABSTRACT

Surface oxygen vacancy defects and metal deposition on semiconductor photocatalysts play a critical role in photocatalytic reactions. In this work, oxygen-deficient Bi_2WO_6 microspheres have been prepared by a facile ethylene glycol-assisted solvothermal method. Bi^0 nanoparticles were reduced by *in situ* thermal-treatment on Bi_2WO_6 microspheres to obtain $Bi^0@Bi_2WO_{6-x}$ as well as maintaining the oxygen vacancies (OVs) under N_2 atmosphere. Afterwards, photocatalytic NO oxidation removal activities of these photocatalysts were investigated under visible light irradiation and $Bi^0@Bi_2WO_{6-x}$ shows the best NO removal activity than other samples. The photogenerated charge separation and transfer are promoted by Bi^0 nanoparticles deposited on the surface of semiconductor catalysts. OVs defects promote the activation of reactants (H_2O and O_2), thereby enhancing the formation of the active substance. Moreover, both OVs defects and Bi^0 metal have the characteristics of extending light absorption and enhancing the efficient utilization of solar energy. Besides, the photocatalytic NO oxidation mechanism of $Bi^0@Bi_2WO_{6-x}$ was investigated by *in situ* FTIR spectroscopy for reaction intermediates and final products. This work furnishes insight into the synthesis strategy and the underlying photocatalytic mechanism of the surface-modified $Bi^0@Bi_2WO_{6-x}$ composite for pollutants removal.

Recent investigations have shown that the formation of oxygen vacancy defects is considered an effective method for adjusting the semiconductor band gap and its electronic structure [1–3], thereby enhancing visible light absorption [4–6]. Research has confirmed that the construction of oxygen vacancies (OVs) defect promote the activation of reactants (H_2O and O_2), thereby enhancing the formation of the active substance [7,8]. In addition, it is also a well-established phenomenon that the catalytic performance of the photocatalysts can improve by depositing metal nanoparticles due to its surface plasmon resonance (SPR) effect [9–13]. Compared with precious metals, low-cost Bi^0 nanoparticles also can produce SPR effect [14,15], which can enhance the visible light adsorption. Furthermore, Bi^0 metal as a cocatalyst on the surface of the semiconductor can effectively accelerate the charge-carrier separation. Thus, it is of considerable significance to develop a simple and feasible method for constructing OVs and depositing Bi^0 nanoparticles on the surface of the photocatalyst to improve its photocatalytic performance.

As a typical visible-light-driven photocatalyst, Bi_2WO_6 can be excited by the light with a wavelength less than 460 nm, which merely occupies a little fraction of the visible light [16–19]. Moreover, the fast recombination of photogenerated electron-hole pairs also significantly decrease the photocatalytic efficiency of the pristine Bi_2WO_6 [20]. Therefore, expanding the wavelength range of light absorption and promoting the separation of photoinduced charges are two effective methods for enhancing the photocatalytic activity of Bi_2WO_6 [21].

In this work, a convenient and effective *in situ* thermal-treatment method was used to simultaneously construct oxygen vacancies and load Bi^0 nanoparticles on the surface of Bi_2WO_6 microspheres. In the thermal treatment process, Bi^{3+} was reduced by the carbon species on the sample surface and Bi^0 nanoparticles was loaded on the surface of the Bi_2WO_{6-x} microspheres under N_2 atmosphere. The presence of oxygen vacancies and the metal SPR effect can increase the utilization of light and reduce the recombination of photogenerated carriers. Subsequently, photocatalytic NO oxidation removal was investigated under visible light

---

[*] Corresponding authors.
E-mail addresses: huanlu@snnu.edu.cn (H. Lu), jianzhigao@snnu.edu.cn (J. Gao), zgq2006@snnu.edu.cn (G. Zhu).

https://doi.org/10.1016/j.cclet.2020.10.002
1001-8417/

irradiation to evaluate the photocatalytic performance of these obtained photocatalysts.

A solvothermal method with the assisted of ethylene glycol was conducted in order to prepare Bi_2WO_6 microspheres. The synthesis process is in Text S1 (Supporting information). Then, the obtained Bi_2WO_6 was thermal-treated at different temperatures (260, 300, 350, 400 and 450 °C, respectively) in a nitrogen surrounding for 2 h. Moreover, the thermal-treated samples were named as BWO-260, BWO-300, BWO-350, BWO-400, and BWO-450, respectively, and pristine Bi_2WO_6 was designated as BWO. In addition, the Bi_2WO_6 powders synthesized with deionized water as solvents are named as BWO-DW.

As shown in Fig. 1a, all diffraction peaks of the pristine BWO can be indexed to the orthorhombic russellite phase of Bi_2WO_6 (PDF No. 73-2020), and no peak of impurity was observed. With the increasing of the thermal treatment temperature to 450 °C, the characteristic peaks of metal bismuth phase that can be accurately indexed to the hexagonal phase of Bi^0 (PDF No. 44-1246). Moreover, with the thermal treatment temperature increased, the color of the synthesized samples gradually darkens from white to black. The above results indicate that Bi^0 metal phase was increased gradually with the increasing thermal treatment temperature.

FT-IR spectra were employed to further characterize these samples prepared by different solvents, as shown in Fig. S1a (Supporting information). The peaks in BWO spectrum over the range of 2800–3000 cm^{-1} matched the antisymmetrical and symmetrical vibrations of $-CH_2$ [22]. The peaks at 1385 and 1086 cm^{-1} can be attributed to the C—OH and C—O bending vibrations [23,24], respectively. However, the vibration of the chemical bond or functional group related to the C element cannot be detected in the BWO-DW sample (Text S4 and Fig. S1 in Supporting information). As shown in Fig. S1b, X-ray diffraction (XRD) patterns also prove that without Bi^0 metal phase will appear after thermal treatment if there is no organic carbon adsorbed on the sample surface. In Fig. 1b, the organic carbon adsorbed on the BWO catalyst surface has been significantly reduced after the thermal treatment process. Therefore, the organic solvent used in the synthesis of BWO is essential for the reduction of Bi^0 metal from BWO by *in situ* method. The characteristics absorption bands of pristine BWO sample can be observed in the range of 400–800 cm^{-1} (Fig. 1b), which are originated from the Bi-O stretching vibrations, W—O stretching vibrations and W—O—W bridge stretching modes [25,26]. These peaks still exist after BWO thermal treatment at different temperatures, which also indicates that the structure of BWO has not changed during the process of generating Bi^0 phase.

Based on the Bi 4f spectrum of pristine BWO (Fig. 1c), the peaks around 159.05 and 164.35 eV could be ascribed to Bi^{3+} $4f_{7/2}$ and Bi^{3+} $4f_{5/2}$ spin-orbit splitting photoelectrons states being in Bi^{3+} chemical state [14,27], respectively. However, two newly peaks located at 157.8 and 163.25 eV were observed in BWO-350, which are according to the Bi^0 $4f_{7/2}$ and Bi^0 $4f_{5/2}$, respectively. The two peaks are resulted by part of the Bi^{3+} reduced to Bi^0 phase during thermal treatment process, which also confirm the presence of Bi^0 metal phase after thermal treatment [15]. Furthermore, the Bi 4f peak of the BWO-350 sample shows a slight shift towards higher binding energy due to the altering of the electron distribution near the Bi atom [28]. As shown in Fig. 1d, the asymmetric O 1s X-ray photoelectron spectroscopy (XPS) spectrum of BWO can be fitted to three gaussian peaks at 529.75, 530.45 and 531.3 eV, which are ascribed to the lattice oxygen, oxygen vacancies and surface chemisorbed oxygen of BWO [29–31], respectively. The formation of Bi^0 nanoparticles also causes the increasing of oxygen vacancies over BWO-350 during thermal treatment, which is well consistent with the electron paramagnetic resonance (EPR) results in Fig. 1f.

Pristine BWO exhibited an intrinsic visible light absorption edge of approximately 460 nm (Fig. 1e). Interestingly, the samples after thermal-treated exhibited appearance redshift and evident amelioration in visible light absorption compared to pristine BWO. With the thermal treatment temperature increased, photocatalysts exhibited strong absorption in the visible-near infrared (vis-NIR) region due to the OVs and the SPR effect originated from the Bi^0 metal on the semiconductor surface [32]. However, ultraviolet-visible diffuse reflectance spectrum (UV–vis DRS) in Fig. S3c (Supporting information) shows that the BWO-DW sample without obvious redshift as well as optical absorption changes after thermal treatment at different temperatures (Text S6 and Fig. S3 in Supporting information).

EPR analysis was performed to determine the presence of oxygen vacancy visually. As illustrated in Fig. 1f, BWO, BWO-260, BWO-300 and BWO-350 samples exhibit a symmetric EPR signal gradient at about g = 2.003 attributing to the electrons trapped on the oxygen vacancies, where the EPR signal gradually increases

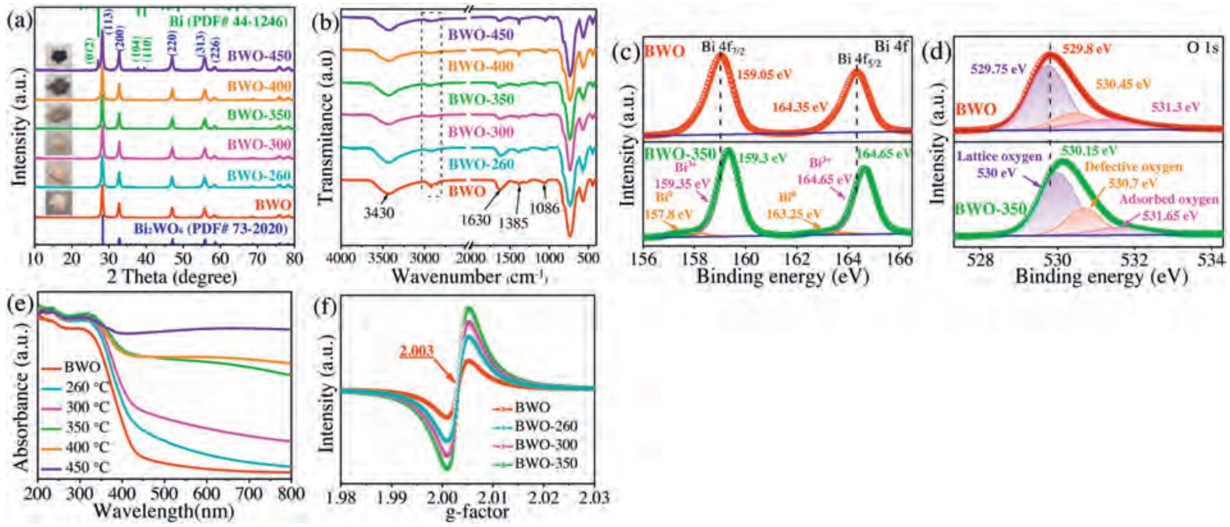

Fig. 1. XRD patterns (a) and FT-IR spectra (b) of the samples synthesized at different thermal treatment temperatures. High-resolution XPS spectra of Bi 4f (c) and O 1s (d) of BWO and BWO-350 samples. (e) UV–vis spectra of the sample with different thermal treatment temperatures. (f) EPR spectra of BWO, BWO-260, BWO-300 and BWO-350 samples.

with the increase of thermal treatment temperature [27,28]. These results indicate that the samples after thermal-treated has more oxygen vacancies. In addition, the thermal-treatment has little effect on the specific surface area and pore size distribution of the samples (Text S6 and Fig. S3d).

It can be observed from the scanning electron microscopy (SEM) and transmission electron microscopy (TEM) images in Figs. 2a-c and Fig. S4 (Supporting information) that all the prepared samples exhibit a self-assembled microsphere morphology composed of nanosheets with a thickness about 6−7 nm. From the SEM image of BWO-450 in Fig. 2b, it can be seen that some irregular nanoparticles loaded on the microspheres. In addition, the high resolution TEM (HRTEM) image of BWO-450 in Fig. 2d displays that the lattice fringes is about 0.315 nm, which matching the (113) crystal plane of Bi_2WO_6 crystal. The energy-dispersive spectroscopy (EDS) results in Fig. S5 and Text S7 (Supporting information) also demonstrate that the Bi^0 particles were produced on the surface of BWO photocatalyst during the process of thermal-treatment. According the above discussion and analysis, the generation of Bi^0 particles and OVs in the BWO during the thermal treatment are illustrated Fig. 2e.

In this study, the NO photocatalytic removal performances of the photocatalysts were investigated under visible light irradiation ($\lambda \geq 420$ nm). Fig. 3a displays the variation of NO concentration with the illumination time of all samples under visible light irradiation. As shown in Fig. S6b (Supporting information), the photocatalytic removal efficiencies of NO oxidation removal over these samples of BWO, BWO-260, BWO-300, BWO-350, BWO-400 and BWO-450 photocatalysts were about 46.5%, 50.5%, 51.3%, 53.4%, 45.1% and 33.1%, respectively. Among them, the BWO-350 sample exhibited the best photocatalytic performance, which may be attributed to the OVs and Bi^0 nanoparticles with enhanced light utilization and effective charge transfer. In order to further confirm whether OVs and Bi^0 nanoparticles both have enhanced light utilization and effective charge transfer, the results of controlling a single variable are provided (Text S9 and Figs. S7a-e in Supporting information). The results show that for the synthesized samples, the presence of OVs and Bi^0 can indeed enhance the effective absorption and utilization of light and the separation and transfer of photogenerated carriers. It also proved that the in-situ synthesized $Bi^0@Bi_2WO_{6-x}$ containing oxygen vacancies has better photocatalytic efficiency than the general chemical loading method. Moreover, the BWO-350 sample has good photocatalytic recyclability and structure stability (Text S10 and Figs. S8a and b in Supporting information).

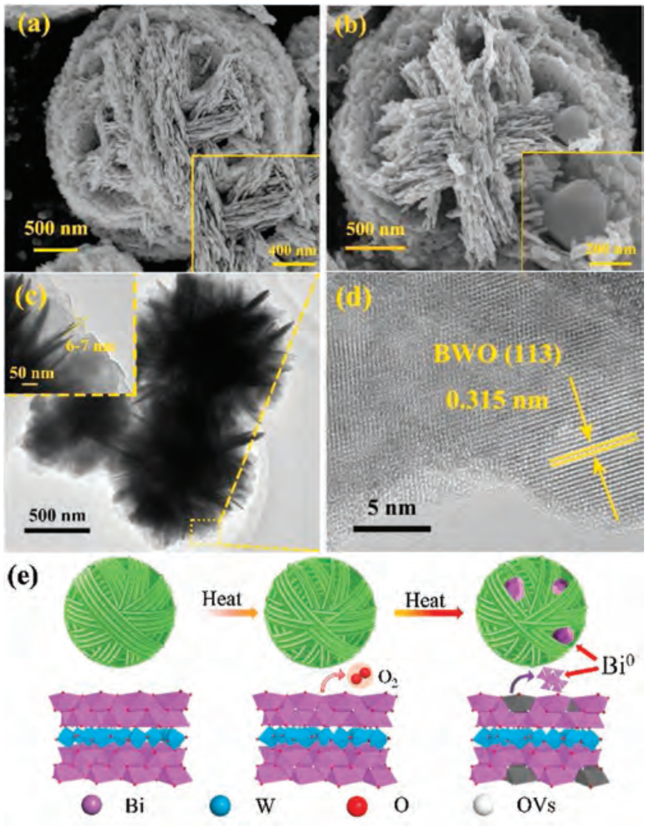

Fig. 2. SEM images of BWO (a) and BWO-450 (b) samples. TEM image (c) and HRTEM image (d) of BWO-450. (e) Schematic diagram of the generation of OVs and Bi^0 nanoparticles during the thermal treatment process.

In order to investigate the photocatalytic mechanism, active substance trapping experiments were performed. As shown in Fig. 3b, the addition of $K_2Cr_2O_7$ into the reaction system obviously reduces the photocatalytic efficiency of BWO-350. In addition, the addition of *p*-benzoquinone (PBQ), KI and isopropanol (IPA) also have a certain influence on the photocatalytic efficiency of the BWO-350 photocatalyst. The trapping experiments results indicated that the electrons, holes, $O_2^{\bullet-}$ and $^{\bullet}OH$, especial the electrons, play a great role in the photocatalytic NO removal. Electron spin resonance (ESR) spectra were further to verify the presence of $O_2^{\bullet-}$ and $^{\bullet}OH$ in the system under visible light illumination over BWO-350 photocatalyst. From Figs. 3c and d, there is no signal under dark condition, indicating no active radicals. However, under visible light irradiation, the characteristic peaks of DMPO-$^{\bullet}OH$ and DMPO-$O_2^{\bullet-}$ are clearly detected, which indicating that both active substances participated in the photocatalytic NO removal process. The ESR spectra are well consistent with the trapping experiments results.

The photoluminescence (PL) spectra, photocurrent, electrochemical impedance spectroscopy (EIS) measurements and surface photovoltage spectroscopy (SPS) were conducted to analyze the separation efficiency of photo-induced electron-hole pairs of the samples (Text S11 and Fig. S9 in Supporting information). Compared with other samples, the photo-induced carriers of BWO-350 sample have lower recombination rate, faster transmission rate, and higher separation efficiency. Therefore, the BWO-350 shows better photocatalytic activity than other samples.

In situ FTIR spectra were used to monitor the adsorption and reaction of NO and O_2 gases on the BWO-350 catalyst surface. Under the dark condition (Fig. 3e), the absorption bands at 987, 1005 and 1059 cm^{-1} are matched the vibration of the bridging nitrate and the bidentate nitrate (NO_2^-) [33], while 1085, 1131 and 1160 cm^{-1} can be ascribed to the vibration of NO gas adsorbed on the surface of photocatalyst [3,33,34]. The absorption peak at 1365 cm^{-1} is ascribed to NO_2 due to the part of NO oxidized to NO_2 under dark condition (Eq. 1) [3]. Furthermore, the absorption bands at 1105, 1394, 1457 and 1641 cm^{-1} can be properly allocated to *trans*-hyponitrites ($N_2O_2^{2-}$), monodentate nitrites, linear nitrites, and NO_3^- (Eqs. 2 and 3) [27,35], respectively. The intensity of the peaks at 1394 and 1641 cm^{-1} increased slightly over time. The possible reaction paths are shown in the following equations (Eqs. 1–3):

$$2NO + O_2 \rightarrow 2NO_2 \quad (1)$$

$$2NO + O_2 + O^{2-}\ (OVs) \rightarrow NO_2^- + NO_3^- \quad (2)$$

$$4NO + 2O^{2-} \rightarrow 2NO_2^- + [N_2O_2]^{2-} \quad (3)$$

Fig. 3f shows the photocatalytic NO oxidation process of the BWO-350 sample under visible light irradiation. After light

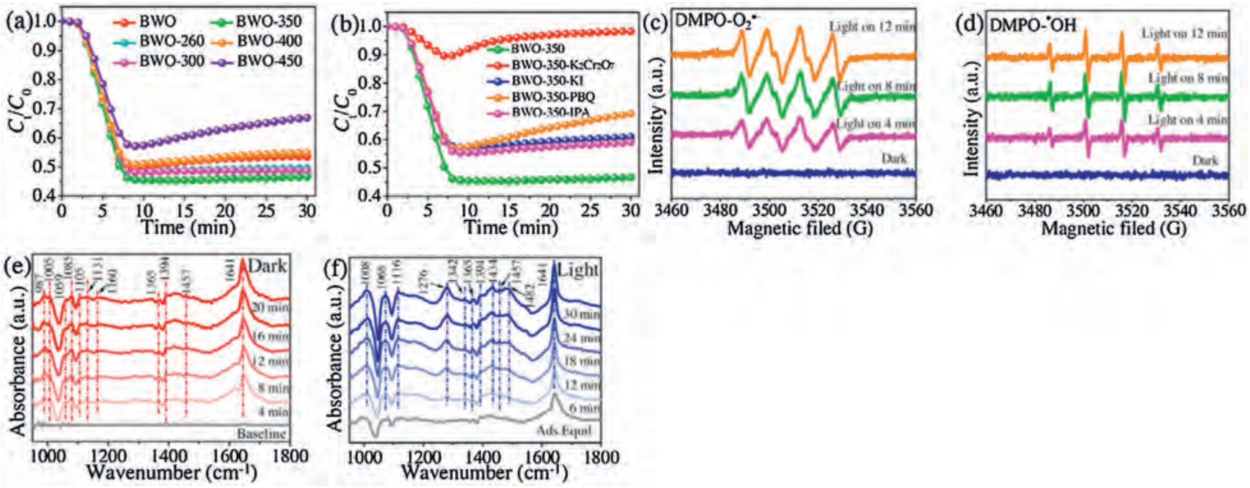

Fig. 3. (a) Photocatalytic activity under visible light irradiation for the samples undergone at different thermal-treatment temperatures. (b) Photocatalytic activities of BWO-350 photocatalyst in the presence of various scavengers. (c) DMPO-$O_2^{\bullet-}$ spectra and (d) DMPO-$^{\bullet}OH$ spectra of the BWO-350 sample under visible light irradiation. *In situ* FTIR spectra under dark condition (e) and visible light (f) reaction processes over BWO-350.

irradiation, a series of new absorption bands at 1008, 1068, 1116, 1276, 1342, 1434 and 1482 cm^{-1} can be detected. The absorption bands at 1116, 1342, and 1482 cm^{-1} could be originated from the bridge nitrites and bidentate nitrates [27,35,36]. Also, the absorption bands at 1008, 1068, 1276 and 1434 cm^{-1} can be assigned to *cis*-($N_2O_2^{2-}$), NO^-, monodentate nitrates and NO^{2-} (chelated) [7,15,27,37], respectively. The absorption bands allocated to nitrate species increased significantly with irradiation time. After light on, e^- and h^+ are generated by photoexcited and react with O_2 and OH^- on the catalyst surface to form $O_2^{\bullet-}$ and $^{\bullet}OH$, respectively. Then, the reaction between the NO gas on the catalyst surface and various reactive species is switched in the direction of formation of more stable nitrates. The possible reaction paths of the whole process of photocatalysis are as following (Eqs. 4–11):

$$\text{BWO-350} + h\nu \rightarrow e^- + h^+ \quad (4)$$

$$NO_2 + e^- \rightarrow NO_2^- \quad (5)$$

$$NO + e^- \rightarrow NO^- \quad (6)$$

$$O_2 - e^- \rightarrow O_2^{\bullet-} \quad (7)$$

$$NO + O_2^{\bullet-} \rightarrow NO_3^- \quad (8)$$

$$NO^- + O_2^{\bullet-} \rightarrow NO_3^- \quad (9)$$

$$OH^- + h^+ \rightarrow {}^{\bullet}OH \quad (10)$$

$$NO^- + {}^{\bullet}OH \rightarrow NO_3^- \quad (11)$$

Based on the discussions made above, a probable mechanism diagram of the improved photocatalytic performance of $Bi^0@Bi_2WO_{6-x}$ is shown in Fig. 4. Under visible light irradiation, the electrons in the valence band (VB) of Bi_2WO_{6-x} semiconductor are excited to undergo energy level transitions, generating photogenerated carriers. Due to the SPR effect, Bi^0 metal nanoparticles also can generate hot electrons to participate in redox reactions. In this way, O_2 adsorbed on the photocatalyst surface can capture electrons and react to form the active species $O_2^{\bullet-}$, and then NO and $O_2^{\bullet-}$ react more effectively to form nitrates. In addition, holes in the VB of Bi_2WO_{6-x} can oxidize OH^- to the active species $^{\bullet}OH$. In summary, the enhanced photocatalytic removal of NO by as-synthesized samples is mainly due to the synergistic effect of Bi^0 nanoparticles and oxygen vacancies.

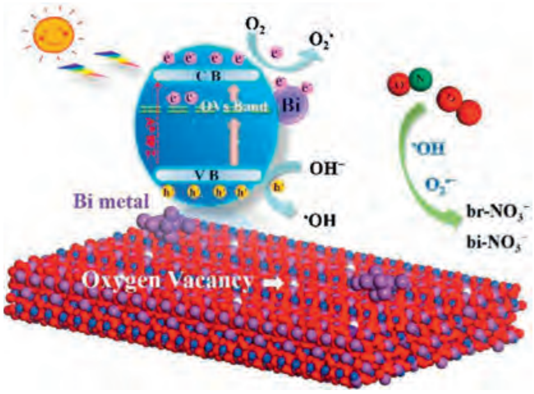

Fig. 4. Mechanism of processes occurring during visible-light-driven photocatalytic NO removal over $Bi^0@Bi_2WO_{6-x}$.

In summary, Bi_2WO_6 microspheres were prepared by a simple hydrothermal method, and then Bi^0 nanoparticles loaded on Bi_2WO_{6-x} with oxygen vacancies were prepared by thermal treatment method under N_2 atmosphere condition. The existence of OVs and Bi^0 nanoparticles not only increases the visible light utilization of the photocatalyst but also enhances the separation and transfer efficiency of photogenerated electron-hole pairs. The photocatalytic performance of $Bi^0@Bi_2WO_{6-x}$ significantly improved by the synergetic effect of the presence of appropriate Bi^0 nanoparticles content and surface oxygen vacancies. Our work employs a new approach towards controlling oxygen vacancies and Bi^0 metal nanoparticles loaded on the surface of semiconductor catalysts.

Declaration of competing interest

The authors declare that they have no known competing financial interests or personal relationships that could have appeared to influence the work reported in this paper.

Acknowledgments

This work was supported by the National Natural Science Foundation of China (No. 51772183), the key Research and Development Program of Shaanxi Province (No. 2018ZDCXL-SF-02-04), and the Fundamental Research Funds for the Central Universities (Nos. GK201903023 and GK201801005).

Appendix A. Supplementary data

Supplementary material related to this article can be found, in the online version, at doi:https://doi.org/10.1016/j.cclet.2020.10.002.

References

[1] J.Y. Zhang, G.Q. Zhu, S.P. Li, et al., ACS Appl. Mater. Interfaces 11 (2019) 37822–37832.
[2] C.W. Yuan, W. Cui, Y.J. Sun, et al., Chin. Chem. Lett. 31 (2020) 751–754.
[3] F. Rao, G.Q. Zhu, W.B. Zhang, et al., Appl. Catal. B: Environ. 281 (2021)119481.
[4] Y.F. Jia, S.P. Li, H.X. Ma, et al., J. Hazard. Mater. 382 (2020) 121121.
[5] H.Q. Tan, Z. Zhao, W.B. Zhu, et al., ACS Appl. Mater. Interfaces 6 (2014) 19184–19190.
[6] L. Nie, J.Z. Gao, Q. Shen, et al., Sci. China Mater. 63 (2020) 2272–2280.
[7] Z.H. Cui, X.A. Dong, Y.J. Sun, et al., Nanoscale 10 (2018) 16928–16934.
[8] Z.D. Wei, R. Wang, Chin. Chem. Lett. 27 (2016) 769–772.
[9] M.Q. Yang, M.M. Gao, M.H. Hong, G.W. Ho. Adv. Mater. 30 (2018) 1802894.
[10] C. Liang, C.G. Niu, L. Zhang, et al., J. Hazard. Mater. 361 (2019) 245–258.
[11] L.B. Chang, G.Q. Zhu, Q, et al., Langmuir 35 (2019) 11265–11274.
[12] Y.Z. Chen, Z.Y.U. Wang, H.W. Wang, et al., J. Am. Chem. Soc. 139 (2017) 2035–2044.
[13] R.B. Wei, P.Y. Kuang, H. Cheng, et al., ACS Sustain. Chem. Eng. 5 (2017) 4249–4257.
[14] X.W. Li, W.D. Zhang, J.Y. Li, et al., Appl. Catal. B: Environ. 241 (2019) 187–195.
[15] X.W. Li, W.D. Zhang, W. Cui, et al., Chem. Eng. J. 370 (2019) 1366–1375.
[16] H. Chen, C.Y. Zhang, Y. Pang, et al., RSC Adv. 9 (2019) 22559–22566.
[17] L.B. Xiao, R.B. Lin, J. Wang, et al., J.Colloid Interface Sci. 523 (2018) 151–158.
[18] J. Di, C. Chen, C. Zhu, et al., Appl. Catal. B: Environ. 238 (2018) 119–125.
[19] H.M. Zhang, J. He, C.Y. Zhai, M.S. Zhu, Chin. Chem. Lett. 30 (2019) 2338–2342.
[20] J.G. Hou, S.Y. Cao, Y.Z. Wu, et al., Nano Energy 32 (2017) 359–366.
[21] Y.B. Chen, J.F. Li, P.Y. Liao, et al., Chin. Chem. Lett. 31 (2020) 1516–1519.
[22] J. Ni, J.J. Xue, L.F. Xie, et al., Phys. Chem. Chem. Phys. 20 (2018) 414–421.
[23] Q.L. Fang, B.L. Chen, J. Mater. Chem. A 2 (2014) 8941–8951.
[24] T.N. Reddy, J. Manna, R.K. Rana, ACS Appl. Mater. Interfaces 7 (2015) 19684–19690.
[25] J.G. Yu, J.F. Xiong, B. Cheng, et al., J. Solid State Chem. 178 (2005) 1968–1972.
[26] S.Y. Wang, H. Yang, Z. Yi, X.X. Wang. J. Environ. Manag. 248 (2019) 109341.
[27] W.C. Huo, X.A. Dong, J.Y. Li, et al., Chem. Eng. J. 361 (2019) 129–138.
[28] X.Y. Kong, Y.Y. Choo, S.P. Chai, et al., Chem. Commun. 52 (2016) 14242–14245.
[29] C.W. Yuan, W. Cui, Y.J. Sun, et al., Chin. Chem. Lett. 31 (2020) 751–754.
[30] S. He, C. Yan, X.Z. Chen, et al., Appl. Catal. B: Environ. 276 (2020) 119138.
[31] S.Y. Zhu, W.R. Liao, M.Y. Zhang, S.J. Liang, Chem. Eng. J. 361 (2019) 461–469.
[32] S. Patnaik, S. Martha, G. Madras, K. Parida, Phys. Chem. Chem. Phys. 18 (2016) 28502–28514.
[33] G.G. Jiang, X.W. Li, M.N. Lan, et al., Appl. Catal. B: Environ. 205 (2017) 532–540.
[34] G.Q. Zhu, M. Hojamberdiev, S.L. Zhang, et al., Appl. Surf. Sci. 467-468 (2019) 968–978.
[35] H. Li, X.Q. Yan, B. Lin, et al., Nano Energy 47 (2018) 481–493.
[36] J.W. Cao, J.Y. Zhang, X.A. Dong, et al., Appl. Catal. B: Environ. 249 (2019) 266–274.
[37] H. Wang, W.J. He, X.A. Dong, et al., Sci. Bull. (Beijing) 63 (2018) 117–125.